

Theory of Spin Injection in Two-dimensional Metals with Proximity-Induced Spin-Orbit Coupling

Yu-Hsuan Lin,¹ Chunli Huang,^{2,3} Manuel Offidani,⁴ Aires Ferreira,⁴ and Miguel A. Cazalilla^{1,3,5}

¹*Department of Physics, National Tsing Hua University, Hsinchu 30013, Taiwan*

²*Department of Physics, The University of Texas at Austin, Austin, Texas 78712, USA*

³*National Center for Theoretical Sciences (NCTS), Hsinchu 30013, Taiwan*

⁴*University of York, Department of Physics, YO10 5DD, York, United Kingdom*

⁵*Donostia International Physics Center (DIPC),*

Manuel de Lardizabal, 4. 20018 Donostia-San Sebastian, Spain

Spin injection is a powerful experimental probe into a wealth of nonequilibrium spin-dependent phenomena displayed by materials with spin-orbit coupling (SOC). Here, we develop a theory of coupled spin-charge diffusive transport in two-dimensional spin-valve devices. The theory describes a realistic proximity-induced SOC with both spatially uniform and random components of the SOC due to adatoms and imperfections, and applies to the two dimensional electron gases found in two-dimensional materials and van der Waals heterostructures. The various charge-to-spin conversion mechanisms known to be present in diffusive metals, including the spin Hall effect and several mechanisms contributing current-induced spin polarization are accounted for. Our analysis shows that the dominant conversion mechanisms can be discerned by analyzing the nonlocal resistance of the spin-valve for different polarizations of the injected spins and as a function of the applied in-plane magnetic field.

Layer-by-layer assembly of atomically thin crystals has provided a unique platform to realize emergent phenomena in two dimensional electron systems [1]. Examples range from secondary Dirac points and Hofstadter’s butterfly in Moiré superlattices [2–4] to superconductivity in twisted bilayer graphene [5, 6] and long-lived excitons in heterobilayers made from semiconducting two-dimensional (2D) crystals [7].

The engineering of the electronic properties, and in particular, the strength of spin-orbit coupling (SOC) in layered materials is facilitated by the weak van der Waals bonding that allows the stacking of two-dimensional (2D) crystals with precise interlayer registry [8]. Indeed, several approaches can be used to enhance and control SOC in the two-dimensional electron gases formed at the atomically thin interfaces of 2D crystals and van der Waals heterostructures. Being essentially surfaces, it is possible to decorate them with various kinds of adsorbates that locally induce/enhance the SOC by proximity [12, 32–34]. In addition, SOC can be substantially enhanced by placing graphene layers on semiconducting transition metal dichalcogenides (TMD) monolayers [10, 11, 13–24, 30, 40]. A sizeable and controllable SOC in graphene and other 2D metals provides a rich arena for the study spin transport phenomena that is not accessible in other, more conventional 2D metals such as resonantly-enhanced skew scattering from spin-active impurities [26, 27, 35, 38], or spin-transparent impurities in graphene with noncollinear spin texture [29], as well as anisotropic-spin precession scattering from impurities that induce Rashba-like SOC by proximity [38].

Previous studies have modeled proximity-induced SOC in heterostructures made of graphene on TMDs by treating the interfacial coupling as a perturbation to the band

structure that is compatible with the lattice symmetries of pristine graphene [28–31]. This minimal model treats the proximity-induced SOC as “intrinsic” and reproduces accurately the spin splitting and \mathbf{k} -dependent spin polarization of low-energy states from first-principles calculations [11, 13, 14]. Thus, it may be regarded as an accurate description of ultra-clean heterostructures, where conduction states lie within the band gap of the substrate and are therefore only weakly affected by interfacial SOC. However, a realistic model should also contain a spatially fluctuating SOC component that describes, for example, structural inhomogeneities between the two materials. Moreover, random SOC-active impurities [32, 33] are inevitable even in the cleanest samples [15]. Owing to the Dirac nature of charge carriers in some 2D materials, localized spin-orbit potentials can lead to sharp scattering resonances and thus enhanced skew scattering [35]. The kinetic theory formulated in Ref. [38, 39] describes spin-coherent transport in single-layer graphene containing a dilute ensemble of SOC-active impurities. Notably, current-induced spin polarization (CISP) can arise purely from random SOC [38, 39]: In addition to extrinsic version of the Edelstein effect (EE) [46], a different (direct) mechanism for spin-charge conversion mechanism was also found in Ref. [38]. Termed anisotropic spin precession scattering [38, 39], it is a direct magnetoelectric effect (DMC) which yields an additional contribution to the CISP.

In this work, we study spin injection in spin-valve devices made from 2D metals with SOC induced by proximity. In such devices, we have found that the polarization of the injected spins determines the dominant spin-to-charge conversion mechanism at distances $\sim l_s$ where l_s is the spin-diffusion length. Thus, it is possible to ascer-

tain which mechanism yields the dominant contribution to the nonlocal resistance of the device by controlling the polarization of the injected spins or by analyzing the dependence of the nonlocal resistance with an in-plane magnetic field. The two mechanisms that can contribute to the nonlocal resistance are either the inverse SHE or the inverse CISP (also known as spin-Galvanic effect, SGE). Both mechanisms are the Onsager reciprocal of the SHE and the CISP. However, for sake of simplicity, below we shall refer to them as SHE and CISP.

Furthermore, below we also provide a microscopic derivation from kinetic theory of the spin diffusion equations describing diffusive transport in 2D metals where the proximity-induced SOC contains randomly fluctuating components. To this end, we consider two distinct physical scenarios. First, we consider a model of random SOC induced by impurities. The single-impurity potential is treated by means of the T-matrix approach, which allows us to capture resonant-scattering effects. In a second scenario, the proximity-induced SOC potential consists of a uniform (“intrinsic?” component and a random component, which is treated in the gaussian (i.e. “white noise”) approximation. We show that these two scenarios lead to the same set of drift-diffusion equations, albeit with different values for the transport and spin-charge conversion coefficients. Thus, we expect this set of equations will apply to a fairly broad class of 2D diffusive metals with proximity-induced SOC.

The remainder of the manuscript is organized as follows. In Sec. I, we present the set of drift-diffusion equations that and briefly discuss how they compare to those derived in previous works. In Sec. II, the equations are applied to a non-local spin valve device and the smoking-gun signatures of the charge-to-spin conversion are discussed. Sections III and IV are concerned with the microscopic derivation of the spin-charge coefficients for uniform proximity-induced SOC (Sec. III) and random SOC (Sec. IV).

I. COUPLED SPIN-CHARGE DIFFUSION EQUATIONS

In the diffusive regime where the elastic mean free path ℓ is much larger than the Fermi wavelength k_F^{-1} , the coupled spin-charge dynamics is described by the following set of equations (henceforth summation over repeated indices is implied unless otherwise stated):

$$\partial_t \rho + \partial_i J_i = 0, \quad (1)$$

$$[\nabla_t s]^a + [\nabla_i \mathcal{J}_i]^a = -\Gamma_s^{ab} s^b + \kappa_i^a J_i, \quad (2)$$

$$J_i = -D (\partial_i \rho + \kappa_a^i s^a) + \gamma_{ij}^a \mathcal{J}_j^a, \quad (3)$$

$$\mathcal{J}_i^a = -D [\nabla_t s]^a + \gamma_{ij}^a J_j, \quad (4)$$

where we have used the following notation:

$$[\nabla_i O]^a = \partial_i O^a - \epsilon^{abc} A_i^b O^c, \quad (5)$$

$$[\nabla_t O]^a = \partial_t O^a + \epsilon^{abc} A_0^b O^c. \quad (6)$$

Eqs. (1) and (2) are the continuity equations for the charge carrier density (ρ) and electron’s spin density (s^a , where $a \in \{x, y, z\}$), respectively. Γ_s^{ab} are the (anisotropic) relaxation rates for the spin; J_i and \mathcal{J}_i^a are the charge and spin current densities, respectively, and $i \in \{x, y\}$. Eqs. (3) and (4) are the generalized constitutive relations for the local charge and spin observables; D is the diffusion constant, which we have assumed to be the same for charge and spin (relaxing this assumption only affects our results quantitatively at the cost of introducing additional complexity). The coupling between charge current (J_i), spin current (\mathcal{J}_i^a) and spin density (s^a) is described by two sets of spin-charge conversion rates: γ_{ij}^a controls the magnitude spin Hall effect (SHE), and $\kappa_i^a = -\kappa_a^i$ controls the magnitude of the direct magneto-electric (DMC) coupling [39], a contribution to current-induced spin polarization (CISP) additional to the Edelstein effect (EE) [46]. In addition, the coupling between \mathcal{J}_i^a to s^a is hidden in the covariant derivative defined in Eq. (5). In this equation, A_i^b describes the coupling to the uniform component of the Rashba-type SOC and $A_0^b = g\mu_L \mathcal{H}^b$ describes the Zeeman coupling. The discussion of spin-swapping [58] term in Eq. (4) is relegated to Sec. III since they are not directly related to spin-charge current, and we treat A_i^b , γ_{ij}^a , κ_i^a in Eqs. (3) to (5) phenomenologically since they are model-dependent as shown in Section III and IV.

It is useful to compare the above set of equations, (1) to (4), with those derived in previous work. A similar set of coupled spin-charge diffusion equations were derived for 2D electron gases by means of the Keldysh formalism with SOC treated as a non-Abelian (SU(2)) gauge field in Refs. [42, 52]. However, in addition to the spin-charge conversion mechanisms described therein, Eqs. (2) and (3) also account for the DMC mechanism. The latter describes a (direct) coupling between the charge current, J_i , and the spin polarization, s^a , and it is parametrized by the coefficients $\kappa_i^a = -\kappa_a^i$. We shall show in Secs. III and IV that the DMC can emerge from the scattering of the carriers with the spatially random components of the SOC, and more specifically, from a non-vanishing correlation between in-plane and out-of-plane electric fields at the interface.

In Refs. [44, 55], the spin diffusion equations were derived from the density-density response function. This approach is well suited in the strong SOC regime where the intrinsic SOC is comparable to the Fermi energy, as in the case of surface states of 3D topological insulator [55]. Such strong SOC regime, strictly speaking, lies outside the applicability of the microscopic models discussed in Sec. III and IV and used to derive Eqs. (1) to (4). Nev-

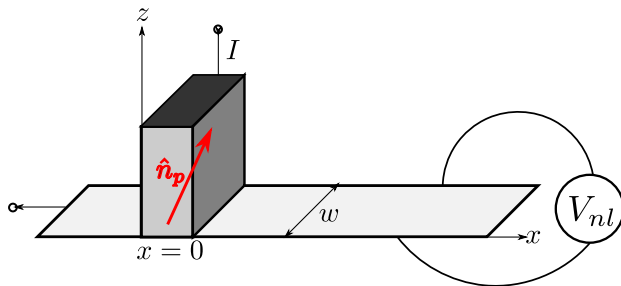


FIG. 1. Illustration of the nonlocal transport device considered in this work. The external magnetic \mathcal{H} field is applied along the y axis, on the plane of the device.

ertheless, on phenomenological grounds, it is worth exploring how such regime can be described starting from the above set of equations. In the strong SOC regime, the spin current is not a hydrodynamic mode of the system and the only relevant spin-charge conversion rate corresponds to κ_i^a in Eq. (2) for the DMC. Thus, upon setting $\gamma_{ij}^a = 0$ in Eq.(3), we recover Eq. 5 of Ref. [55] with $\kappa_i^a = \ell^{-1}\epsilon_i^a$, $\ell = v_F\tau$ (τ) being the elastic mean-free path (elastic scattering time). Finally, we note that a similar set of equations has been obtained for superconductors within the quasi-classical approximation in Refs. [51, 53, 54]. The latter are complicated by the fact that quasi-particle spectral weights are no longer peaked on the Fermi surface and in general are altered by the nonequilibrium dynamics. However, in the normal state, they can be brought to the form of Eqs. (1)-(4).

II. SPIN-VALVE

In this section, our goal is to describe the properties of the nonlocal resistance in a lateral spin-valve device of the type employed to measure the inverse spin Hall effect in the seminal experiments by Valenzuela and Tinkham [62], see Fig. 1 for an illustration of the device.

We shall be concerned with 2D metals that are isotropic in the long wavelength limit, but, due to presence of a substrate or absorbates, have broken mirror reflection symmetry about the 2D plane. This includes van der Waals heterostructures, such as graphene on TMD [56]. From these symmetry considerations, the conversion rates describing the SHE and DMC are given by:

$$\gamma_{ij}^a = \theta_{\text{SH}}\epsilon_{ij}\delta^{az} \quad \kappa_i^a = l_{\text{DMC}}^{-1}\epsilon_i^a, \quad (7)$$

where θ_{SH} is the spin Hall angle and l_{DMC} is a parameter with units of length that determines the conversion efficiency of the DMC ($\epsilon_x^y = \epsilon_y^x = \epsilon_{xy} = -\epsilon_y^x = -\epsilon_x^y = -\epsilon_{yx} = 1$ is the fully anti-symmetric 2D tensor). In addition,

$$A_i^a = l_R^{-1}\epsilon_i^a \quad (8)$$

where the parameter l_R has units of length and parametrizes the strength of the inversion-symmetry breaking Rashba SOC (cf. Sec.III and IV). In order to reduce the number of parameters in the model calculation below, we shall assume that the spin relaxation time to be isotropic: $\Gamma_s^{ab} = \delta^{ab}\tau_s^{-1}$ (i.e. it is the same for the in-plane and out of plane spin components). These assumptions will allow us to derive simple analytical expressions for the nonlocal resistance of the device ((see Ref. ?? for a discussion of the corrections to the nonlocal transport introduced by spin lifetime anisotropy).

In what follows, we shall work in the limit where SOC is weak compared to the Fermi energy of the electron gas. Therefore, the spin diffusion length $l_s = \sqrt{D\tau_s} \gg \ell$. In addition, the dimensionless spin-charge conversion ratios θ_{SH} , l_s/l_{DMC} , and l_s/l_R will be assumed to be small (compared to unity) and therefore contributions of quadratic order in these coefficients can be safely neglected. Under such conditions, the build-up of a non-local voltage in the lateral spin valve (Fig. 1) can be regarded as the result of a three-stage process. First, a finite spin density, $\mathbf{s}(x=0)$, is injected by driving a current I through the ferromagnetic metal contact. Second, the injected spin polarization $\mathbf{s}(x=0)$ diffuses away from the injection point according to Eq. (2). And finally, at a distance x from the injector, $\mathbf{s}(x)$ generates a transverse electric current via Eq. (3) and leads to the appearance of a finite nonlocal voltage, $V_{nl}(x)$. The measured nonlocal resistance, $R_{nl}(x)$ is the ratio $V_{nl}(x)/I$. Notice that, for large SOC, this three stages are not independent and one has to solve Eqs. (1) to (4) self-consistently, see e.g. Ref. [43]. In the following, we shall describe the three stages in detail.

A. Spin-injection

For a ferromagnetic metal contact whose dimensions are much smaller than the spin diffusion length (l_s) in the 2D material, the injected spin density can be described by a single vector $\mathbf{s}(x=0)$ whose direction and magnitude depends on the details of the contact. From the conservation of charge and spin current at the contact, the following boundary conditions are obtained [50]:

$$J_F(z=0) = J(x=0), \quad (9)$$

$$\mathcal{J}_F(z=0) = \hat{\mathbf{n}}_p \cdot [\mathcal{J}_x(x=0^+) - \mathcal{J}_x(x=0^-)]. \quad (10)$$

Here, J_F and \mathcal{J}_F are, the charge and the spin current densities flowing into the 2D metal, respectively, and $\hat{\mathbf{n}}_p = \sin\theta_p \cos\varphi_p \hat{x} + \sin\theta_p \sin\varphi_p \hat{y} + \cos\theta_p \hat{z}$ is the polarization direction of the injected spins near the contact. Eqs. (9) and (10) assume that the contact does not trap charge or accumulate any spin torque. In this situation, the spin polarization of the injected carriers is parallel to

the ferromagnet magnetization. Thus, as we show below, the magnitude of the spin density depends on the applied current I and the contact conductance.

At the contact position (i.e. $x = 0$), the terms proportional to the gradient of the charge and spin densities in the constitutive relations (cf. Eq.(3) and (4)) dominate. Thus, we can approximate

$$J(x=0) \approx -D \frac{d\rho(x)}{dx} \Big|_{x=0}, \quad (11)$$

$$\hat{\mathbf{n}}_p \cdot \mathcal{J}_x(x=0^\pm) \approx -D \frac{d(\mathbf{s}(x) \cdot \hat{\mathbf{n}}_p)}{dx} \Big|_{x=0^\pm}. \quad (12)$$

B. Spin diffusion away from injection

Next, we derive the spin diffusion (Bloch) equation from the set of drift-diffusion equations introduced in Sec. I by eliminating the charge and spin-currents. In addition, we shall assume that the spin channel in the 2D metal has a large length-to-width ratio $L/w \gg 1$ and also $w \ll l_s$, so that the spin relaxation along the transverse direction is suppressed. Within this one-dimensional channel approximation, the resulting spin diffusion equation can be written as follows:

$$\bar{\mathcal{D}} \cdot \mathbf{s}(x) + \omega_L (\hat{\mathbf{n}}_H \times \mathbf{s}(x)) = 0 \quad (13)$$

where

$$\bar{\mathcal{D}} = D \begin{pmatrix} \partial_x^2 - l_s^{-2} & 0 & 2l_R^{-1} \partial_x \\ 0 & \partial_x^2 - l_s^{-2} & 0 \\ -2l_R^{-1} \partial_x & 0 & \partial_x^2 - l_s^{-2} \end{pmatrix} \quad (14)$$

and $\omega_L = g\mu_L |\mathcal{H}|/\hbar$ is the Larmor frequency induced by the magnetic field $\mathcal{H} = |\mathcal{H}| \hat{\mathbf{y}}$, and $\hat{\mathbf{n}}_H = \hat{\mathbf{y}}$.

The general solution to Eq. (13) can be written as follows:

$$s^x(x) = s^x(0) \text{Re } z(x) - s^z(0) \text{Im } z(x) \quad (15)$$

$$s^z(x) = s^z(0) \text{Re } z(x) + s^x(0) \text{Im } z(x). \quad (16)$$

The $s^y(x)$ component decouples from the others and does not contribute to the spin-charge conversion processes (its behavior is discussed in Appendix A). The function $z(x)$ characterizes the oscillatory decay of the two spin components and reads:

$$z(x) = \exp\left(-\kappa|x| + i\frac{x}{l_R}\right), \quad (17)$$

where $\kappa = \sqrt{l_s^{-2} - l_R^{-2} + i\omega_L D^{-1}}$ and the two constants, $s_x(0)$ and $s_z(0)$ are obtained by matching the solution with the boundary conditions, Eqs. (9) and (10). The calculation of $s_x(0)$ and $s_z(0)$ is described in Appendix A. Here it suffices to know that the result depends on the injected current I and the conductance of the junction between the ferromagnetic metal contact and the 2D material.

C. Spin-charge conversion and nonlocal voltage

Next, we use the solution of the spin Bloch equation to obtain the charge current flowing along the y -direction, $J_y(x)$. This transverse electric current generates a voltage drop $V_{\text{nl}}(x)$. The nonlocal resistance is thus defined by the expression:

$$R_{\text{nl}}(x) = \frac{V_{\text{nl}}(x)}{I} = \frac{wJ_y(x)}{I\sigma_N}, \quad (18)$$

where σ_N is the electric conductivity of the device and w is the channel width. The solution of the spin diffusion equations contains three distinct contributions to the nonlocal signal:

$$R_{\text{nl,sH}}(x) = \frac{wD}{I\sigma_N} \theta_{\text{sH}} \partial_x s^z \quad (19)$$

$$R_{\text{nl,EE}}(x) = -\frac{wD}{I\sigma_N} \theta_{\text{sH}} l_R^{-1} s^x \quad (20)$$

$$R_{\text{nl,DMC}}(x) = -\frac{wD}{I\sigma_N} l_{\text{DMC}}^{-1} s^x \quad (21)$$

Experimentally, $R_{\text{nl,EE}}(x)$ and $R_{\text{nl,DMC}}(x)$ cannot be distinguished and therefore we shall combine them into one single contribution to $R_{\text{nl}}(x)$ arising from the current-induced spin polarization (CISP) mechanisms:

$$R_{\text{nl,CISP}}(x) = R_{\text{nl,EE}}(x) + R_{\text{nl,DMC}}(x) \quad (22)$$

In realistic spin-valve measurements, there is always some level of background noise, which masks the pure spin contribution to the nonlocal resistance [62]. The background signal can be eliminated by subtracting the nonlocal resistances between parallel and anti-parallel configurations (see Appendix A for details):

$$\begin{aligned} \Delta R_{\text{nl}}(x) &= R_{\text{nl}}(x) \Big|_{\hat{\mathbf{n}}_p} - R_{\text{nl}}(x) \Big|_{-\hat{\mathbf{n}}_p} \\ &= R_0 C_{\text{inj}} e^{-\tilde{q} \cos \theta_L x} f(\hat{\mathbf{n}}_p, \omega_L) \end{aligned} \quad (23)$$

In the above expression,

$$\tilde{q} = |\kappa| = \frac{1}{l_s} \left[(1 - l_s^2/l_R^2)^2 + (\omega_L \tau_s)^2 \right]^{1/4}, \quad (24)$$

is the characteristic wave number associated with spatial variation of the nonlocal resistance, $\theta_L = \frac{1}{2} \tan^{-1} [\omega_L \tau_s / (1 - l_s^2/l_R^2)] \approx \frac{1}{2} \tan^{-1} (\omega_L \tau_s)$, and $R_0 = (w/l_s) G_F$, where G_F is the conductance of the ferromagnetic metal. The dimensionless parameter C_{inj} characterizes the properties of the junction between the ferromagnet and the 2D material. Typically, the conductance of the normal metal is much smaller than the ferromagnet

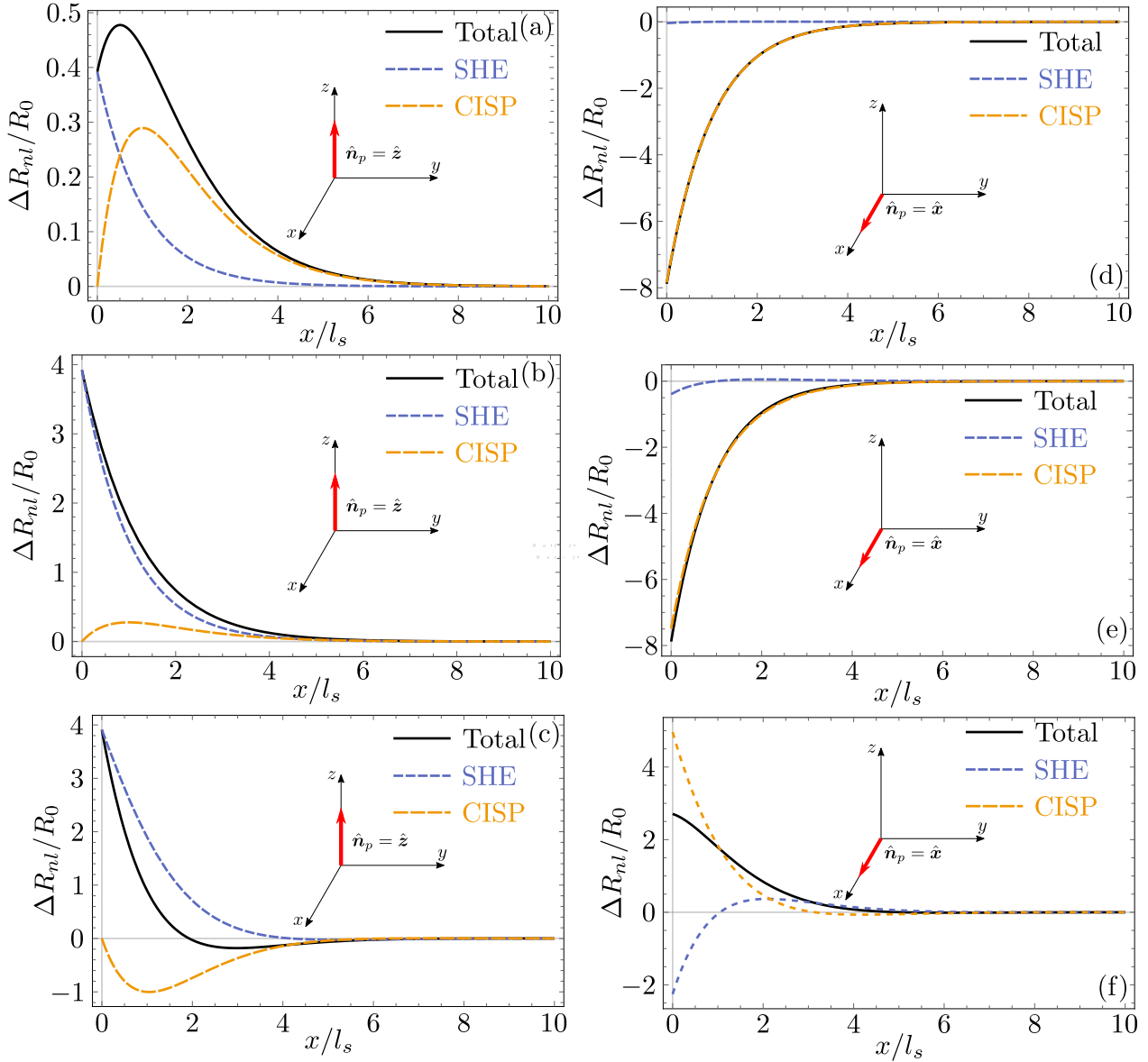


FIG. 2. Nonlocal resistance $R_{nl}(x)$ versus distance from the spin injection contact (x). In panels a,b, and c (d,e, and f) the polarization of the injected spins is perpendicular (parallel) to the plane of the 2D electron gas. The results depend on three spin-charge conversion coefficients, namely the spin-Hall angle θ_{sH} , a length scale associated with the spin precession induced by the Rashba SOC, l_R and a length scale associated with a direct magneto-electric coupling, l_{DMC} . For each panel, we have chosen the following experimentally relevant values: $l_s = 10^{-6}$ m [12]; $\theta_{sH} = -0.01$, $l_R = 2l_{DMC} = 10l_s$ in (a) and (d); $\theta_{sH} = -0.1$, $l_R = 2l_{DMC} = 10l_s$ in (b) and (e); $\theta_{sH} = -0.1$, $l_R = -0.12l_{DMC} = 2l_s$ in (c) and (f); $P_J = 0.4$ [63], $P_F = 0.73$ [64], $G_N/G_F = 0.01$ [65], and $G/G_F = 5 \times 10^{-4}$.

$G_N/G_F \sim 10^{-2}$ (tunneling limit). Thus, in this regime where $G_N \gg G_F$, the injection spin efficiency becomes:

$$C_{inj} \simeq \frac{P_J G_F}{G_N \tilde{q} l_s}. \quad (25)$$

On the other hand, in the transparent limit where $G \gg G_F$,

$$C_{inj} \simeq \frac{2P_F}{1 - P_F^2 \cos \theta_L + (\tilde{q} l_s - \cos \theta_L) \sin^2 \theta_p \sin^2 \varphi_p}. \quad (26)$$

The dimensionless function $f(\hat{n}_p, \omega_L)$ in Eq. (23) describes the interplay between different spin-charge conversion effects, the Larmor precession, and the quantization axis (magnetization direction) of the ferromagnet

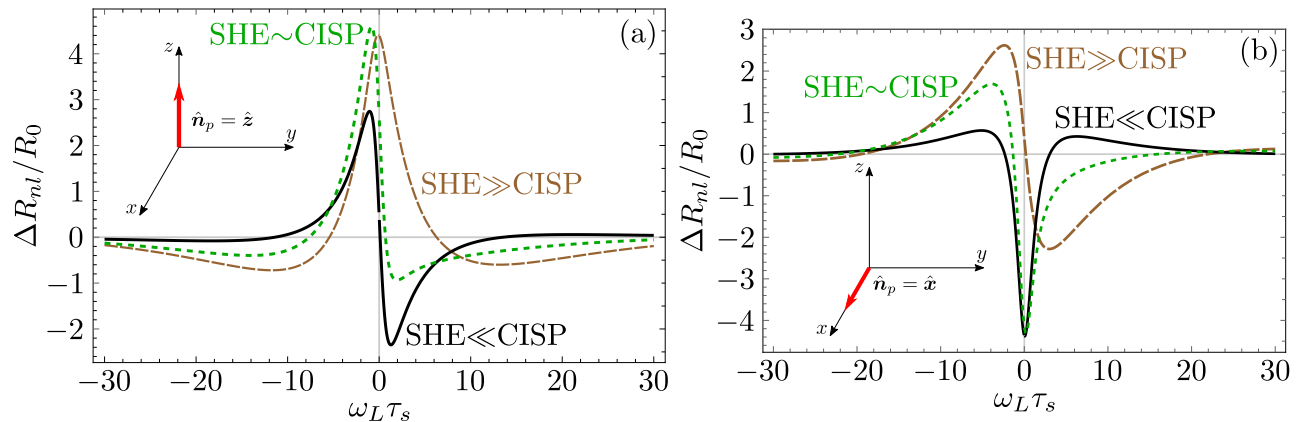


FIG. 3. Nonlocal resistance versus magnetic field (measured in units of the Larmor frequency times the spin relaxation time, i.e. $\omega_L \tau_s$) at $x = l_s$. We take $l_s/l_R = 0.1$ for all curves. The parameters for the solid black curve are $\theta_{\text{SH}} = -10^{-3}$, and $l_s/l_{\text{DMC}} = 0.2$. The parameters for the dashed (brown) curve are $\theta_{\text{SH}} = -0.2$, and $l_s/l_{\text{DMC}} = 2 \times 10^{-3}$. The parameters for the dashed (green) curve are $\theta_{\text{SH}} = -0.1$, and $l_s/l_{\text{DMC}} = 0.2$.

described by \mathbf{n}_p . Its full form is given in Eq. (A13) in Appendix A.

Let us first discuss the main features of the nonlocal resistance in the absence of magnetic field, i.e. $f(\hat{\mathbf{n}}_p, \omega_L = 0)$. It takes the following form for \mathbf{n}_p along the in the x and z axes, respectively:

$$f(\hat{\mathbf{z}}, 0) = -\theta_{\text{SH}} \tilde{q} l_s \cos\left(\frac{x}{l_R}\right) + \frac{l_s}{l_{\text{DMC}}} \sin\left(\frac{x}{l_R}\right) \quad (27)$$

$$f(\hat{\mathbf{x}}, 0) = -\theta_{\text{SH}} \tilde{q} l_s \sin\left(\frac{x}{l_R}\right) - \frac{l_s}{l_{\text{DMC}}} \cos\left(\frac{x}{l_R}\right). \quad (28)$$

From the above expressions, it can be seen that, up to an exponential decay factor (cf. Eq. 23), for $x \ll l_R$, the nonlocal resistance $\Delta R_{\text{nl}}(x) \sim \theta_{\text{SH}}$ for $\hat{\mathbf{n}}_p = \hat{\mathbf{z}}$, whereas $\Delta R_{\text{nl}} \sim l_s/l_{\text{DMC}}$ for $\hat{\mathbf{n}}_p = \hat{\mathbf{x}}$. Thus, at distances much smaller than the typical distance for precession under the Rashba field, l_R , the non-local resistance is approximately proportional to the spin Hall angle θ_{SH} when the injected spins are polarized out of the plane of the device, i.e. for $\hat{\mathbf{n}}_p = \hat{\mathbf{z}}$. On the other hand, the nonlocal resistance is approximately proportional to the ratio l_s/l_{DMC} when the injected spins lie on the plane of the device, i.e. for $\hat{\mathbf{n}}_p = \hat{\mathbf{x}}$. The full spatial dependence of $\Delta R_{\text{nl}}(x)$ for zero magnetic field is shown in Fig. 2. The left panels correspond to out-of-plane polarization ($\hat{\mathbf{n}}_p = \hat{\mathbf{z}}$) whereas the right panels correspond to in-plane polarization ($\hat{\mathbf{n}}_p = \hat{\mathbf{x}}$).

The above observations concerning the behavior of $\Delta R_{\text{nl}}(x)$ at short distances point to possibility of measuring the spin-charge conversion coefficients θ_{SH} and l_s/l_{DMC} or at least experimentally discerning the dominant spin-charge conversion mechanism in a device. Theoretically, these coefficients (together with l_s/l_R) depend on the microscopic details of the model (see Secs. III and IV) and we have treated them phenomenologically. Thus, in Fig. 2, we have plotted $R_{\text{nl}}(x)$ for a wide range

of choices of θ_{SH} , l_s/l_R , and l_s/l_{DMC} . The two contributions to $\Delta R_{\text{nl}}(x)$ arising from the SHE and CISP mechanisms are also displayed in Fig. 2 (dashed lines). Notice that the SHE is dominant for $\hat{\mathbf{n}}_p = \hat{\mathbf{z}}$ and CISP is dominant for $\hat{\mathbf{n}}_p = \hat{\mathbf{x}}$, as noted above. However, this does not mean that the CISP (SHE) contribution is negligible in the former (latter) case. Indeed, a word of caution is necessary since the SHE contribution does not only correspond to the first term ($\propto \tilde{q}\theta_{\text{SH}}$) in the right-hand side of Eqs. (27) and (28)). By the same token, the second term in Eqs. (27) and (28)) does not exactly correspond to the CISP contribution: It arises from the DMC contribution. Indeed, there is an additional term in the expression for the SHE contribution which is equal in magnitude but opposite in sign to the EE contribution to CISP ($\propto \theta_{\text{SH}} l_s/l_R$). This explains why in the bottom right panel the contribution from SHE takes a non-zero value at $x = 0$ despite that the injected spins point along the x -axis. Indeed, $R_{\text{nl},\text{SH}}(x = 0) \sim \partial_x s^x(x = 0) = s^x(0) \text{Im}[\partial_x z(x = 0)] \propto l_s/l_R$. That is, even if the polarization of the spins at $x = 0$ is along the x -axis and therefore $s^z(0) = 0$, the gradient of $s^z(x)$ at $x = 0$ does not vanish and thus the contribution of the SHE is nonzero. This is also visible (although less clearly) in panels Fig. 2(d) and (e).

A few other interesting features of Fig. 2 are noteworthy. For $\hat{\mathbf{n}}_p = \hat{\mathbf{z}}$ (left panels), as the spin Hall angle is increased from $\theta_{\text{SH}} = 0.01$ (panel a) to $\theta_{\text{SH}} = 0.1$ (panel b) while keeping l_s/l_{DMC} constant, the non-monotonic behavior of $\Delta R_{\text{nl}}(x)$ disappears. Indeed, even though the SHE dominates at distances $x \lesssim l_s$ for small spin Hall angle, as noted above, the contribution arising from CISP, which is small for $x \lesssim l_s$ becomes comparable to the SHE contribution for $x \approx l_s$. This is because spins at $x \sim l_s$ spins have undergone relaxation and precession under the Rashba field onto the plane where the DMC

mechanism is most effective. However, as the spin Hall angle is increased to $\theta_{\text{SH}} = -0.1$ (panel b), the contribution from the SHE becomes an order of magnitude larger and it is dominant even for $x \sim l_s$. Thus, the peak in $\Delta R_{nl}(x)$, which results from CISP taking over SHE for $x \sim l_s$, disappears. Finally, at the bottom panel (c) of Fig. 2, we show results with a decreased ratio $l_R/l_s = 2$, which implies that for $x/l_s \sim 1$ the spins undergo a sizable precession in the Rashba field. This enhances the EE contribution to the CISP, which now shows a quantitatively different behavior from panels (a) and (b). For the plots on the right, the spins are injected in plane (along the x -axis, and CISP essentially accounts for most of the nonlocal resistance of the device, even though for the bottom panel ($l_R/l_s = 2$) the Rashba precession gives rise to a sizable contribution from the SHE for $x \lesssim l_s$.

Finally, let us briefly discuss the effect of the applied magnetic field. The dimensionless function $f(\hat{\mathbf{n}}_p, \omega_L)$ takes the following forms when $\hat{\mathbf{n}}_p$ points along the x and z directions, respectively:

$$f(\hat{\mathbf{z}}, \omega_L) = \left[-\theta_{\text{SH}} \tilde{q} l_s - \frac{l_s}{l_{\text{DMC}}} \sin \theta_L \right] \cos \left(\frac{x}{l_{\text{eff}}} \right) + \frac{l_s}{l_{\text{DMC}}} \cos \theta_L \sin \left(\frac{x}{l_{\text{eff}}} \right) \quad (29)$$

$$f(\hat{\mathbf{x}}, \omega_L) = \left[-\theta_{\text{SH}} \tilde{q} l_s - \frac{l_s}{l_{\text{DMC}}} \sin \theta_L \right] \sin \left(\frac{x}{l_{\text{eff}}} \right) - \frac{l_s}{l_{\text{DMC}}} \cos \theta_L \cos \left(\frac{x}{l_{\text{eff}}} \right) \quad (30)$$

where $l_{\text{eff}}^{-1} = l_R^{-1} - \tilde{q} \sin \theta_L$. Thus, at short distances, $\Delta R_{nl} \sim \theta_{\text{SH}} + (\sin \theta_L / \tilde{q} l_s) l_s / l_{\text{DMC}}$ for $\hat{\mathbf{n}}_p = \hat{\mathbf{z}}$. On the other hand, $\Delta R_{nl} \sim \cos \theta_L (l_s / l_{\text{DMC}})$ for $\hat{\mathbf{n}}_p = \hat{\mathbf{x}}$. Recall that $\theta_L \approx \frac{1}{2} \tan^{-1}(\omega_L \tau_s)$, which means that the dominant mechanism at short distance is modified (relative to $\omega_L = 0$) by the Larmor precession in the external magnetic field, as expected.

In Fig. II C, we plot ΔR_{nl} versus the magnitude of applied magnetic field measured in units of the Larmor frequency times the spin relaxation time, i.e. $\omega_L \tau_s$. For $\hat{\mathbf{n}}_p = \hat{\mathbf{z}}$, ΔR_{nl} is almost symmetric because the SHE contribution dominates over CISP. On the other hand, ΔR_{nl} becomes almost anti-symmetric asymmetric when the CISP contribution dominates over the SHE. For $\hat{\mathbf{n}}_p = \hat{\mathbf{x}}$, ΔR_{nl} is highly symmetric when CISP dominates over SHE (i.e. for $\theta_{\text{SH}} \gg l_s / l_{\text{DMC}}$, while ΔR_{nl} is highly asymmetric in the opposite limit where SHE dominates over CISP. Thus, in summary, the symmetry of this curve, combined with the very different behavior of $\Delta R_{nl}(x)$ as a function of the distance x to the injection contact for zero magnetic field and different polarization of the injected spins should provide a ‘‘smoking gun’’ for the dominant spin-charge conversion mechanism in lateral spin-valve devices.

III. PURELY EXTRINSIC SOC

In this section, we derive the set of drift-diffusion equations introduced in Sec. I from a model that assumes purely extrinsic SOC. This model is appropriate to graphene decorated with absorbates. We treat scattering with the absorbates nonperturbatively, which allows to describe resonant scattering effects. The latter is very important in graphene due to appearance of scattering resonances in the neighborhood of the Dirac point. This approximation is valid in the limit of a dilute number of scatterers.

We shall rely on the (linearized) quantum Boltzmann equation (QBE) that describes the dynamics of the 2-by-2 density matrix distribution $n_k(\mathbf{r}, t)$ in spin space and reads:

$$\begin{aligned} \partial_t \delta n_k(\mathbf{r}, t) + (\mathbf{v}_k \cdot \partial_{\mathbf{r}}) \delta n_k(\mathbf{r}, t) \\ + \frac{i}{\hbar} \gamma [\delta n_k(\mathbf{r}, t), \mathbf{s} \cdot \mathcal{H}(t)] + \\ e \mathbf{E}(t) \cdot \frac{\nabla_k n_k^0}{\hbar} = \mathcal{I}[\delta n_k], \end{aligned} \quad (31)$$

In the above expression, the spin operator is given by $\mathbf{s} = \frac{\hbar}{2} \boldsymbol{\sigma}$ where $\boldsymbol{\sigma}$ is the Pauli matrices, and the deviation of the distribution from equilibrium is given by $\delta n_k(\mathbf{r}, t) = n_k(\mathbf{r}, t) - n_k^0$, where $n_k^0 = f_{\text{FD}}[\varepsilon_k] \mathbb{1}$, $f_{\text{FD}}(\varepsilon) = [e^{(\varepsilon - \bar{\mu})/T} + 1]^{-1}$ the Fermi-Dirac distribution at temperature T and chemical potential $\bar{\mu}$, and $a \mathbb{1}$ is the 2×2 identity matrix in spin space. For graphene, the dispersion relation for electron is given by $\varepsilon_k = \hbar v_F k$, $\mathbf{E}(t)$ is the applied electric field, and $\mathcal{H}(t)$ is the applied magnetic field.

The collision integral in the above QBE was derived in Ref. [38] to leading order in the density of impurities, and reads: n_{imp} , is given by the following expression:

$$\begin{aligned} \mathcal{I}[\delta n_k] = \frac{i}{\hbar} [\delta n_k, \text{Re} \Sigma_k] + \frac{2\pi n_{\text{imp}}}{\hbar} \sum_p \delta(\varepsilon_k - \varepsilon_p) \\ \times \left[T_{kp}^+ \delta n_p T_{pk}^- - \frac{1}{2} \left\{ \delta n_k, T_{kp}^+ T_{pk}^- \right\} \right] \end{aligned} \quad (32)$$

The self energy Σ_k^R reads as

$$\text{Re} \Sigma_k^R = \frac{n_{\text{imp}}}{2} (T_{kk}^+ + T_{kk}^-) \quad (33)$$

In order to derive the drift-diffusion equations, we use the following ansatz to solve the QBE:

$$\begin{aligned} n_k^0 + \delta n_k(\mathbf{r}, t) = f_{\text{FD}}[\varepsilon_k - \mu(\mathbf{r}, t) - h_0 \boldsymbol{\sigma} \cdot \mathbf{n}_0(\mathbf{r}, t) \\ - \hbar \mathbf{k} \cdot \mathbf{v}_c(\mathbf{r}, t) - \hbar \mathbf{k} \cdot \mathbf{v}_s(\mathbf{r}, t) (\boldsymbol{\sigma} \cdot \mathbf{n}_1(\mathbf{r}, t))] \end{aligned} \quad (34)$$

In what follows, we shall look for a solution of the QBE to linear order in μ , h_0 , \mathbf{v}_c , \mathbf{v}_s , and μ . Here $\mu(\mathbf{r}, t)$ is the

local deviation from the average chemical potential, $\bar{\mu}$; $\mathbf{v}_c(\mathbf{r}, t)$ ($\mathbf{v}_s(\mathbf{r}, t)$) is the local drift velocity of the charge (spin); $\mathbf{n}_0(\mathbf{r}, t)$ ($\mathbf{n}_1(\mathbf{r}, t)$) is the polarization direction of the nonequilibrium magnetization (spin current). The parameters in the above ansatz are related to the charge density $\rho(\mathbf{r}, t)$, spin density $\mathbf{s}(\mathbf{r}, t)$, charge density current $\mathbf{J}(\mathbf{r}, t)$, and spin current density $\mathcal{J}^a(\mathbf{r}, t)$ by the following expressions:

$$\begin{aligned}\rho(\mathbf{r}, t) &= \frac{g_s g_v}{2\Omega} \sum_k \text{Tr} [\delta n_k(\mathbf{r}, t)] \\ &= g_s g_v N_0 \mu(\mathbf{r}, t)\end{aligned}\quad (35)$$

$$\begin{aligned}\mathbf{s}(\mathbf{r}, t) &= \frac{g_s g_v}{2\Omega} \sum_k \text{Tr} [\boldsymbol{\sigma} \delta n_k(\mathbf{r}, t)] \\ &= g_s g_v N_0 h_0 \mathbf{n}_0(\mathbf{r}, t)\end{aligned}\quad (36)$$

$$\begin{aligned}\mathbf{J}(\mathbf{r}, t) &= \frac{g_s g_v}{2\Omega} \sum_k \text{Tr} [\delta n_k(\mathbf{r}, t)] \mathbf{v}_k \\ &= g_s g_v \frac{N_0}{2} \varepsilon_F \mathbf{v}_c(\mathbf{r}, t)\end{aligned}\quad (37)$$

$$\begin{aligned}\mathcal{J}^a(\mathbf{r}, t) &= \frac{g_s g_v}{2\Omega} \sum_k \text{Tr} [\sigma^a \delta n_k(\mathbf{r}, t)] \mathbf{v}_k \\ &= g_s g_v \frac{N_0}{2} \varepsilon_F \mathbf{v}_s(\mathbf{r}, t) n_1^a(\mathbf{r}, t)\end{aligned}\quad (38)$$

Here g_s and g_v are spin degeneracies and valley degeneracies respectively, N_0 is the density of states per spin per valley at the Fermi surface. In evaluating the sums over momentum above, we have assumed the low-temperature limit where $T \ll \bar{\mu}$ and approximated $\partial_\epsilon n_k^0 \simeq -\delta(\epsilon_k - \epsilon_F)$ where $\varepsilon_F = \bar{\mu}(T=0)$ is the Fermi energy.

Note in Eq. (37) and (38), the currents are given by the first moment of deviation from equilibrium of the distribution function. In the presence of SOC, they are *not*

the conserved current that enters the continuity equation. The conserved current is a sum of two distinct contributions: the first moment excitation of the Fermi surface and the anomalous current which arises from evaluating the collision integral to order $k_F^{-1} \nabla_r$ [54]. In fact, the anomalous current contributes precisely to the so-called side-jump contribution, see Ref. [51] for more in-depth discussion. However, if we limit ourselves to study spin-charge coefficients to the leading order in impurity density n_{imp} , the collision integral in Eq. (70) is sufficient and the conserved currents are still given by Eq. (37) and (38).

Next, we compute the (retarded) T -matrix for a single impurity. The latter is a 2×2 matrix in spin space, which can be written as follows:

$$T_{kp}^+ = C_{kp} \mathbb{1} + \mathbf{B}_{kp} \cdot \boldsymbol{\sigma} \quad (39)$$

where the coefficients C_{kp} and \mathbf{B}_{kp} are given by:

$$C_{kp} = \gamma_0 \cos\left(\frac{\theta_k - \theta_p}{2}\right) \quad (40)$$

$$\begin{aligned}\mathbf{B}_{kp} &= \gamma_R \sin\left(\frac{\theta_k + \theta_p}{2}\right) \hat{x} - \gamma_R \cos\left(\frac{\theta_k + \theta_p}{2}\right) \hat{y} \\ &\quad + i\gamma_I \sin\left(\frac{\theta_k - \theta_p}{2}\right) \hat{z}\end{aligned}\quad (41)$$

This parametrization of T -matrix follows from symmetry considerations. It respects the rotation generated by total angular momentum (spin angular momentum + orbital angular momentum), in-plane parity and time-reversal symmetry but breaks $z \rightarrow -z$ symmetry.

For a given single-impurity T -matrix, the equations of motion for the different moments of the distribution function (Eq. (35)-(38)) can be obtained to leading order in the impurity density. This involves taking the zeroth and first moments of Eq. (31) followed by the trace of the result over the spin indices. Those manipulations yield the following set of equations:

$$\partial_t \rho(\mathbf{r}, t) + \partial_i J_i(\mathbf{r}, t) = 0 \quad (42)$$

$$\partial_t \mathbf{s}(\mathbf{r}, t) + \partial_i \mathcal{J}_i(\mathbf{r}, t) + \gamma \mathcal{H}(t) \times \mathbf{s}(\mathbf{r}, t) = \mathcal{Q}(\mathbf{r}, t) \quad (43)$$

$$\partial_t J_i(\mathbf{r}, t) + \frac{v_F^2}{2} \partial_i \rho(\mathbf{r}, t) - \frac{\sigma_D}{\tau_c} E_i(t) = -\frac{J_i(\mathbf{r}, t)}{\tau_c} + \alpha_{\text{sk}} \varepsilon_{ij} \mathcal{J}_j^z(\mathbf{r}, t) + \alpha_{\text{asp}} v_F \varepsilon_{ij} s^j(\mathbf{r}, t) \quad (44)$$

$$\partial_t \mathcal{J}_i^a(\mathbf{r}, t) + \frac{v_F^2}{2} \partial_i s^a(\mathbf{r}, t) + \gamma [\mathcal{H}(t) \times \mathcal{J}_i(\mathbf{r}, t)]^a = \chi_i^a(\mathbf{r}, t) \quad (45)$$

The components of $\mathcal{Q}(\mathbf{r}, t)$ and $\chi_i^a(\mathbf{r}, t)$, as well as the

scattering rates are given in Appendix B.

To proceed further, we set $\partial_t J_i = \partial_t \mathcal{J}_i^a = 0$ as corresponds to the steady state. Hence, the constitutive relations for the charge $J_i(\mathbf{r})$ and spin $\mathcal{J}_i^a(\mathbf{r})$ current densities are derived from the Eqs. (44) and (45):

$$J_i = -D\partial_i\rho + \sigma_D E_i + \theta_{\text{SH}}\varepsilon_{ij}\mathcal{J}_j^z + \alpha_{\text{asp}}\tau_c v_F \varepsilon_{ij} s^j \quad (46)$$

$$\mathcal{J}_i^z = -D\partial_i s^z + \theta_{\text{SH}}\varepsilon_{ij} J_j + \alpha_{\text{R}}\tau_c v_F s^i \quad (47)$$

$$\mathcal{J}_x^x = -D'\partial_x s^x - \alpha_{\text{R}}^\perp \tau_c' v_F s^z - \alpha_{\text{LD}}\tau_c' \mathcal{J}_y^y \quad (48)$$

$$\mathcal{J}_y^y = -D'\partial_y s^y - \alpha_{\text{R}}^\perp \tau_c' v_F s^z - \alpha_{\text{LD}}\tau_c' \mathcal{J}_x^x \quad (49)$$

$$\mathcal{J}_x^y = -D''\partial_x s^y + \alpha_{\text{LD}}^\perp \tau_c'' \mathcal{J}_y^x \quad (50)$$

$$\mathcal{J}_y^x = -D''\partial_y s^x + \alpha_{\text{LD}}^\perp \tau_c'' \mathcal{J}_x^y \quad (51)$$

Here $\theta_{\text{SH}} = \alpha_{\text{sk}}\tau_c$ is the spin-Hall angle, and the diffusion constants are given by $D = \frac{1}{2}v_F^2\tau_c$, $D' = \frac{1}{2}v_F^2\tau_c'$, $D'' = \frac{1}{2}v_F^2\tau_c''$.

In order to further simplify the calculations, we shall take $\tau_c = \tau_c' = \tau_c''$. and $\alpha_{\text{R}} = \alpha_{\text{R}}^\perp$ since they differ by terms that are proportional to the SOC induced by the impurities, which are typically small compared to the scalar potential term. In addition, we shall drop the terms proportional to α_{LD} and α_{LD}^\perp , which describe the Lifshitz-Dyakonov spin swapping effect [58]. For $\alpha_{\text{LD}}\tau_c \ll 1$, this effect leads to corrections that are second order in the spin-charge conversion coefficients. The latter, as pointed out above, are typically smaller than one in spintronic devices. Thus, second order effects are negligible and can be neglected. The resulting equations can be brought to the form of Eqs. (3) and (4) with the following choice of parameters:

$$\gamma_{ij}^a = \alpha_{\text{sk}}\tau_c \varepsilon_{ij} \delta^{az} \quad (52)$$

$$(53)$$

$$A_i^b = \frac{2\alpha_{\text{R}}}{v_F} \varepsilon_i^b = l_{\text{R}}^{-1} \varepsilon_i^b \quad (54)$$

$$\kappa_i^a = \frac{2\alpha_{\text{asp}}}{v_F} \varepsilon_i^a = l_{\text{DMC}}^{-1} \varepsilon_i^a \quad (55)$$

$$\Gamma_s^{xx,yy} = \frac{1}{\tau_{\text{EY}}} \quad (56)$$

$$\Gamma_s^{zz} = \frac{1}{\tau_{\text{EY}}^\perp} \quad (57)$$

and $\Gamma^{ab} = 0$ for $a \neq b$. The detailed forms of α_{sk} , α_{R} , α_{asp} , τ_{EY} , τ_{EY}^\perp in terms of the scattering rates with the impurities are given in Appendix B.

By relying on the one-dimensional approximation introduced in Sec. II, the diffusion equation for the spin

density \mathbf{s} in the presence of a weak external magnetic field ($\omega_L\tau_c \ll 1$) can be written as follows:

$$\bar{\mathcal{D}}\mathbf{s}(x) - \omega_L[\hat{\mathbf{n}}_H \times \mathbf{s}(x)] = \mathcal{S}(x), \quad (58)$$

where \mathcal{S} is the source term:

$$\mathcal{S}(x) = \left(2\alpha_{\text{asp}} \frac{J_y(x)}{v_F}, -2\alpha_{\text{asp}} \frac{J_x(x)}{v_F}, \theta_{\text{SH}}\partial_x J_y(x) \right), \quad (59)$$

The diffusion matrix $\bar{\mathcal{D}}$ is

$$\bar{\mathcal{D}} = \begin{pmatrix} D'\partial_x^2 - \frac{1}{\tau_{\text{EY}}} & 0 & \theta_{\text{R}}v_F\partial_x \\ 0 & D''\partial_x^2 - \frac{1}{\tau_{\text{EY}}} & 0 \\ -\theta_{\text{R}}v_F\partial_x & 0 & D\partial_x^2 - \frac{1}{\tau_{\text{EY}}} \end{pmatrix}, \quad (60)$$

where $\theta_{\text{R}} = \tau_c\alpha_{\text{R}} + \tau_c'\alpha_{\text{R}}^\perp$. The above diffusion matrix can be reduced to Eq. (14) if we assume $\tau_{\text{EY}} = \tau_{\text{EY}}^\perp$ in order to simplify the model, as explained in Sec. II.

Furthermore, concerning the source term, screening ensures that the charge density is uniform for length scales larger than the Thomas-Fermi screening length. Therefore, to leading order in the spin-charge conversion coefficients, the charge current density $J \approx -D\nabla\rho + \sigma_D E = 0$ and hence $\mathcal{S}(x) = 0$ in the bulk of the device described in Sec. II.

IV. INTRINSIC SOC WITH RANDOM FLUCTUATIONS

In this section, we shall describe the proximity induced SOC as field consisting of a spatially uniform (i.e. a ‘intrinsic’ SOC) part and a random component that varies slowly in space. Thus, the spin-charge diffusion equations can be derived from a kinetic theory that treats the SOC as a non-abelian gauge field [28, 42, 52]. Remarkably, the resulting diffusion equations take the universal form as those introduced in Eq. (1) - (4). In what follows, we first generalized the celebrated 2D Rashba model [66] to account for smoothly varying SOC potential then, a gauge-covariant kinetic theory is introduced to derive the diffusion equations.

Let us consider a 2D electron gas with Rashba SOC (the so-called Rashba model) and re-write the SOC as time-independent uniform non-abelian gauge-field:

$$H_{\text{R}} = \frac{\mathbf{p}^2}{2m} + \alpha(\boldsymbol{\sigma} \wedge \mathbf{p}) = \sum_{i=x,y} \frac{(p_i - \mathcal{A}_i)^2}{2m} + \text{const.} \quad (61)$$

Here $\mathbf{a} \wedge \mathbf{b} = \varepsilon_{ij} a_i b_j$, and α is the strength of uniform (intrinsic) part of the SOC whilst \mathcal{A}_i is the non-abelian gauge field:

$$\mathcal{A}_i = \sum_{a=x,y,z} \mathcal{A}_i^a \sigma_a. \quad (62)$$

For Rashba SOC, the only non-vanishing components are $\mathcal{A}_y^x = -\mathcal{A}_x^y = m\alpha$. In the literature on proximity effects in 2D metals, it is often assumed that proximity-induced SOC is uniform in space and therefore $[p_j, \mathcal{A}_i] = 0$. Thus, the violation of momentum conservation that is needed in order for the system to reach the steady state is assumed to be driven by scattering with impurities. However, as emphasized above, a realistic SOC induced by proximity should contain both uniform and spatially random components. Thus, in order to account for the random spatial fluctuations, we have generalized the Rashba model introduced above in Eq. (61) by introducing an electrostatic potential $\phi(\mathbf{r})$ and shifting the gauge field as $\mathcal{A}_i \rightarrow \mathcal{A}_i + \delta\mathcal{A}_i(\mathbf{r})$, which yields the following model:

$$H = \sum_{i=x,y} \frac{(p_i - \mathcal{A}_i - \delta\mathcal{A}_i(\mathbf{r}))^2}{2m} + \phi(\mathbf{r}) \quad (63)$$

The potential $\phi(\mathbf{r})$ is a slowly varying function in space and its spatial variation gives rise to finite electric field that generates SOC. In fact, the spatially varying gauge-field is induced by the gradient of the electrostatic potential $\phi(\mathbf{r})$:

$$\delta\mathcal{A}_i^z(\mathbf{r}) = m\alpha_1\epsilon_{ij}\partial_j\phi(\mathbf{r}), \quad (64)$$

$$\delta\mathcal{A}_i^j(\mathbf{r}) = m\alpha_2\epsilon_i^j\partial_z\phi(\mathbf{r}) \quad (65)$$

Here $\partial_z\phi = \partial_z\phi(\mathbf{r}, z)|_{z=0}$ where $z = 0$ is the material plane; $\alpha_1 \sim \alpha$ ($\alpha_2 \sim \alpha$) are material-dependent coefficients that characterize the strength of SOC induced by in-plane (out-of-plane) electric field ($\mathbf{E} = -\nabla\phi$). Note that the generalized Hamiltonian Eq. (63) breaks translational symmetry but retains all other symmetries of the Rashba Hamiltonian Eq. (61).

In order to proceed further, it is convenient to isolate the part that breaks translation symmetry from the Rashba Hamiltonian: $H = H_R + U(\mathbf{r}, \mathbf{p})$ where H_R is given in Eq. (61) and

$$U(\mathbf{r}, \mathbf{p}) = -\frac{1}{2m} \{p_i, \delta\mathcal{A}_i(\mathbf{r})\} + \phi(\mathbf{r}). \quad (66)$$

We have dropped the subleading term $\propto (\delta\mathcal{A}_i)^2$ since it is $\sim \alpha^2$ and small compared to the other two. The matrix elements of this potential are:

$$U_{\mathbf{k}\mathbf{p}} = \phi_{\mathbf{k}-\mathbf{p}} \left\{ 1 + i\alpha_1 (\mathbf{k} \wedge \mathbf{p}) \sigma^z - \frac{\alpha_2}{2\xi} [(\mathbf{p} + \mathbf{k}) \wedge \boldsymbol{\sigma}] \right\}, \quad (67)$$

where $\phi_{\mathbf{k}-\mathbf{p}}$ is the Fourier component of the electric potential and we have approximated $\partial_z\phi \approx \phi/\xi$. Here ξ is a typical length scale of variation in the direction out of the 2D plane. The resulting potential is similar to those described in Refs. [28, 60, 61],

We shall consider the situation where both the fluctuating and uniform components of the SOC are small compared to the Fermi energy $\alpha_1 p_F^2 \sim \alpha_2 p_F/\xi \sim \alpha/v_F \ll 1$.

In this limit, starting from the structure of Eq. (63), one can write down a kinetic equation for the (spin) density-matrix distribution function $n_{\mathbf{k}}(\mathbf{r}, t)$ by relying on gauge invariance (cf. Ref. [41, 42, 53]):

$$(\nabla_t n_{\mathbf{k}} + \mathbf{v}_{\mathbf{k}} \cdot \nabla_{\mathbf{r}} n_{\mathbf{k}}) + \frac{1}{2} \{ \mathbf{F}_{\mathbf{k}}, \partial_{\mathbf{k}} n_{\mathbf{k}} \} = I[\delta n_{\mathbf{k}}]. \quad (68)$$

The intrinsic SOC (i.e. the non-abelian gauge field) modifies the left hand side (dissipation-less part) of the kinetic equation in two essential ways: First, it turns the space-time derivatives into covariant derivatives: $\nabla_{\mathbf{r}}$ (∇_t) is the covariant space (time) derivative that describes the precession of electron spin induced by SOC (external magnetic field). Mathematically, the covariant derivatives on the right hand-side of the kinetic equation have a structure is identical to Eq. 5. However, as we shall see later, the non-abelian gauge connections are renormalized by the fluctuating part of the SOC. Second, $\mathbf{F}_{\mathbf{k}}$ is the non-abelian generalization of external applied force acting on electron \mathbf{k} . The three spatial components of the non-abelian force are obtained from $F_{\mathbf{k}}^j = V_a \mathcal{F}^{aj}$ where $(V_a) = (1, v_{x\mathbf{k}}, v_{y\mathbf{k}}, 0)$ is the four-velocity and $\mathcal{F}^{ab} = \partial^a \mathcal{A}^b - \partial^b \mathcal{A}^a - [\mathcal{A}^a, \mathcal{A}^b]$ is the field strength tensor. Here the indices $j = x, y, z$ while the indices $a, b = t, x, y, z$. For example, if we submit an electric field \mathbf{E} in the presence of Rashba SOC with gauge-field $\mathcal{A}_y^x = -\mathcal{A}_x^y = m\alpha$, the resulting non-abelian force contains a spin-dependent Lorentz force responsible for the intrinsic spin Hall effect [67]:

$$\mathbf{F}_{\mathbf{k}} = e\mathbf{E} + \mathbf{v}_{\mathbf{k}} \times (e\mathbf{B}_s) \quad (69)$$

where $\mathbf{B}_s = (8m^2\alpha^2/e^2)\sigma^z\hat{\mathbf{z}}$ is the spin-dependent magnetic.

The potential $\phi(\mathbf{r})$ is treated as a random potential, which contributes to the relaxation of momentum and spin and therefore must be described by the collision integral of the kinetic equation. The collision integral to second order in $\delta\mathcal{A}$, in the self-consistent Born-approximation, takes the form:

$$\begin{aligned} \mathcal{I}[\delta n_{\mathbf{k}}] &= \frac{i}{\hbar} [\delta n_{\mathbf{k}}, \text{Re} \Sigma_{\mathbf{k}}^{\text{B}}] + \frac{2\pi}{\hbar} \sum_{\mathbf{p}} \delta(\epsilon_{\mathbf{k}} - \epsilon_{\mathbf{p}}) \\ &\times \left[\overline{U_{\mathbf{k}\mathbf{p}} \delta n_{\mathbf{p}} U_{\mathbf{p}\mathbf{k}}} - \frac{1}{2} \{ \delta n_{\mathbf{k}}, \overline{U_{\mathbf{k}\mathbf{p}} U_{\mathbf{p}\mathbf{k}}} \} \right], \quad (70) \end{aligned}$$

where $\Sigma_{\mathbf{k}}^{\text{B}}$ is the hermitian part of the self-energy:

$$\text{Re} \Sigma_{\mathbf{k}}^{\text{B}} = \overline{U_{\mathbf{k}\mathbf{k}}} + P \int \frac{d^2q}{(2\pi)^2} \frac{\overline{U_{\mathbf{k}q} U_{q\mathbf{k}}}}{\epsilon - \epsilon_q} \quad (71)$$

Here $\overline{O[\phi]} = \sum_{\phi} P[\phi] O[\phi]$ and $P[\phi]$ is the probability distribution function of the random potential ϕ . For simplicity, we assume they are distributed according to Gaussian distribution with zero mean:

$$\overline{\phi_{\mathbf{q}}} = 0 \quad (72)$$

$$\overline{\phi_{\mathbf{q}_1} \phi_{\mathbf{q}_2}} = n_s v_0^2 \delta^2(\mathbf{q}_1 + \mathbf{q}_2) \quad (73)$$

The parameter n_s has dimensions of inverse length square and is akin to n_{imp} in Sec. III; v_0 is the typical energy scale of the random part of the proximity induced electric potential $\phi(\mathbf{r})$. Since $\phi(\mathbf{r})$ has zero mean value, the first term in Eq. (71) vanishes under potential average. However the second term does not vanish and still contributes to the energy shift. Then, unlike the uniform gauge field \mathcal{A}_i , the fluctuating gauge-field $\delta\mathcal{A}_i$ generates dissipation and enters the kinetic theory via the collision integral. For a potential $\phi(\mathbf{r})$ with short-range correlations, the collision integral in Eq. (70) suffices to describe the spin-charge relaxation since it accounts for the matrix structure of the disorder potential, i.e. Eq. (66). However, it is still an approximation because Eq. (70) does not account for the modification of the scattering states by the uniform part of the SOC $\mathcal{A}_i \sim \alpha$: The asymptotic scattering states are given by spin-independent Bloch waves with energy $\epsilon_k = v_F k$. This is consistent with our assumption of a weak SOC with our treatment of the left-hand side of Eq. (68), which is valid to second order in α .

After using the same ansatz as in Eq. (34) to solve the above kinetic equation, we arrive at the set of drift-diffusion equations, Eqs. (1) to (4) with the following identification for the parameters:

$$\gamma_{ij}^a = \frac{8m\alpha^2}{\pi n_s N_0 v_0^2} \frac{\epsilon_{ij} \delta^{az}}{\left(2 + \alpha_1^2 k_F^4 + 2 \left(\frac{\alpha_2}{2\xi}\right)^2 k_F^2\right)} \quad (74)$$

$$A_i^b = \left[\mathcal{A}_y^x - \frac{4mn_s}{\pi \hbar v_F} v_0^2 \left(\frac{\alpha_2}{2\xi}\right)^2 \ln\left(\frac{q_c}{k_F}\right) \right] \epsilon_i^b \quad (75)$$

$$\kappa_i^a = \frac{4\pi n_s}{\hbar v_F} N_0 v_0^2 \alpha_1 \left(\frac{\alpha_2}{2\xi}\right) k_F^3 \epsilon_i^a \quad (76)$$

$$\Gamma_s^{xx,yy} = \frac{1}{\tau_s^{x,y}} \quad (77)$$

$$= \frac{2\pi n_s}{\hbar} N_0 v_0^2 \left[2 \left(\frac{\alpha_2}{2\xi}\right)^2 k_F^2 + \alpha_1^2 k_F^4 \right] \quad (78)$$

$$\Gamma_s^{zz} = \frac{1}{\tau_s^z} = \frac{8\pi n_s}{\hbar} N_0 v_0^2 \left(\frac{\alpha_2}{2\xi}\right)^2 k_F^2 \quad (79)$$

In the above equations, k_F is the Fermi momentum, and $q_c \sim k_F$ is high-momentum cut-off. Note that the total gauge-field A_i^b appearing in the diffusion equation receives contributions from both the uniform gauge field (\mathcal{A}_y^x) and the fluctuating gauge field ($\delta A \propto n_s v_0^2$).

V. SUMMARY

In this work, we have extended the theory of spin-injection in 2D metals to account for proximity induced

spin-orbit coupling (SOC). The theory relies on a set of diffusion equations that capture the two main types of mechanisms for spin-charge conversion, namely the spin Hall effect (SHE) and the current-induced spin polarization (CSIP). For the latter, two kinds of contributions have been identified and accounted for: the Edelstein effect, which generates a spin polarization via the SHE coupled with spin precession caused by the Rashba SOC, and the direct magneto electric coupling (DMC). The latter describes a direct coupling between the spin polarization and the electric current, which can arise in systems with random SOC. We would like to emphasize that such random SOC should be generically present in 2D metals with proximity induced SOC.

Our calculations for a lateral spin-valve device allowed us to identify the SHE and CSIP contributions to the non-local resistance of the device. Thus, we have been able to ascertain the conditions under which, by changing the quantization axis of the injected spins, the observed nonlocal signal is dominated by one of the two spin-charge conversion mechanism mentioned above.

In addition, we have provided a microscopic derivation of the diffusion equations. This has been achieved by treating the describing the proximity-induced SOC in two physically distinct limits. In one of them, we have assumed that SOC is induced by spatially localized impurities. This limit is applicable e.g. to graphene randomly decorated with adsorbates (or clusters thereof). In the other limit, we have assumed that SOC consist of a uniform part plus a random component, which is appropriate to 2D heterostructures of graphene or another two-dimensional metal placed on transition metal dichalcogenides, for instance. We have show that the resulting set of equations is identical, which suggests that the coupled spin-charge diffusive equations derived here apply to a broad class of 2D materials in the metallic regime.

The theory presented here can be extended in a number of directions: For instance, accounting for the anisotropy in the spin relaxation should be relatively easy at the expense of introducing an additional (anisotropy) parameter, and also for a moderate spin valley coupling in graphene/TMD heterostructures which can be described as a valley dependent Zeeman coupling.

MAC and YHL have been supported by the Ministry of Science and Technology (Taiwan) under contract number NSC 102- 2112-M-007-024-MY5. MAC also acknowledges the support of the National Center for Theoretical Sciences of Taiwan. A.F. gratefully acknowledges the financial support from the Royal Society, London through a Royal Society University Research Fellowship. M.O. and A.F. acknowledge funding from EPSRC (Grant Ref: EP/N004817/1).

Appendix A: Solution of the Bloch equation

In this section, we provide the details of the calculation leading to the dimensionless parameters, C_{inj} and $f(\hat{\mathbf{n}}_p, \omega_L)$, is given. The solution to the spin-diffusion equation, Eq. (13) is displayed in Eqs. (16). The equation for s^y is decoupled from those of s^x and s^z and its solution reads $s^y(x) = s^y(0)e^{-x/l_s}$.

Since the injected spin of polarization is along the polarization direction $\hat{\mathbf{n}}_p$ of the ferromagnet, the problem of enforcing the boundary conditions (cf. Eqs. (9) and (10)) is largely simplified by projecting the spin current density along $\hat{\mathbf{n}}_p$ on both sides of the ferromagnet-2D material junction, i.e.

$$\begin{aligned} \mathcal{J}_N(x=0) &= \sum_{\sigma} \sigma \mathcal{J}_N^{\sigma}(x=0) \\ &\approx -2D\hat{\mathbf{n}}_p \cdot \partial_x \mathbf{s}(x=0) \end{aligned} \quad (\text{A1})$$

$$\mathcal{J}_F(z=0) = \sum_{\sigma} \sigma \mathcal{J}_F^{\sigma}(z=0) \quad (\text{A2})$$

Here $\mathcal{J}_N^{\sigma}(x=0)$ and $\mathcal{J}_F^{\sigma}(z=0)$ are the spin current density in the channel $\sigma = \pm 1$ ($+$ \equiv \uparrow , $-$ \equiv \downarrow), which points in the direction $\sigma\hat{\mathbf{n}}_p$. Note that we neglect any interfacial spin-flip scattering, so that the polarization of the total spin-current flowing into the 2D metal is parallel to the polarization of the spin current in the ferromagnet:

$$[\mathcal{J}_N(x=0^+) - \mathcal{J}_N(x=0^-)] \parallel \hat{\mathbf{n}}_p \quad (\text{A3})$$

Since non-local resistance must depend on several junction properties such as interfacial conductance, interfacial current polarization, and the current polarization within the ferromagnetic metal, we construct the following electrochemical potential model with two channels pointing in $\pm\hat{\mathbf{n}}_p$ direction respectively in ferromagnetic metal and 2D metal in order to capture the influence of junction properties:

$$\mu_N^{\sigma}(x) = \bar{\mu}_N(x) + \frac{\sigma}{2N_e} \mathbf{s}(x) \cdot \hat{\mathbf{n}}_p \quad (\text{A4})$$

$$\mu_F^{\sigma}(z) = \frac{e^2 I}{\sigma_F A_J} z + eV_1 + b\sigma \left(\frac{\sigma_F}{\sigma_F^{\sigma}} \right) e^{-z/\lambda_F}, \quad (\text{A5})$$

where $\bar{\mu}_N(x) = \frac{e^2 I}{w\sigma_N} x$ for $x < 0$, $\bar{\mu}_N(x) = 0$ for $x > 0$, V_1 is the voltage drop between the ferromagnet and the 2D metal, A_J is the cross section of the ferromagnetic metal, N_e is the density of states per spin when the system is

at equilibrium, λ_F is the spin-diffusion length in the ferromagnet, σ_F^{σ} is the spin-dependent electric conductivity of the ferromagnet, and $\sigma_F = \sigma_F^{\uparrow} + \sigma_F^{\downarrow}$ is the total electric conductivity in the ferromagnet. The electrochemical potential Eqs. (A4) and (A5) are constructed within the guideline that the spin current density projected onto channel σ should be given by the following:

$$\mathcal{J}_{N(F)}^{\sigma} = -\frac{\sigma_N^{\sigma(F)}}{e} \partial_r \mu_{N(F)}^{\sigma} \quad (\text{A6})$$

To proceed further, we assume that the spin current projected onto the quantum axis, I_s , is continuous and arrive at the following equations:

$$I_s = w [\mathcal{J}_N(x=0^+) + \mathcal{J}_N(x=0^-)] \quad (\text{A7})$$

$$I_s = A_J \mathcal{J}_F(z=0^+) \quad (\text{A8})$$

Next, the spin current in each channel stems from the drop of electro-chemical potential between ferromagnetic metal and 2D metal is given by $I_I^{\sigma} = (G^{\sigma}/e^2) [\mu_F^{\sigma}(z=0) - \mu_N^{\sigma}(x=0)]$. The total spin current and charge current are thus given by:

$$I = \sum_{\sigma} I_I^{\sigma} \quad (\text{A9})$$

$$I_s = \sum_{\sigma} \sigma I_I^{\sigma} \quad (\text{A10})$$

Finally, by solving Eqs. (A3), (A7), (A8), (A9), (A10), we arrive at the solutions of $\mathbf{s}(0)$, b , and I_s . Then, the difference in the nonlocal resistance between quantum axis pointing in $\hat{\mathbf{n}}_p$ and quantum axis pointing in $-\hat{\mathbf{n}}_p$ can be evaluated by plugging the solution of $s^x(0)$ and $s^z(0)$ into the following equation:

$$\begin{aligned} R_{\text{nl}}(x) &= \frac{wJ_y(x)}{I\sigma_N} \\ &= \frac{wD}{I\sigma_N} [\theta_{\text{sH}} \partial_x s^z(x) - (\theta_{\text{sH}} l_R^{-1} + l_{\text{DMC}}^{-1}) s^x(x)] \\ &= R_{\text{nl,sH}} + R_{\text{nl,EE}} + R_{\text{nl,DMC}} \end{aligned} \quad (\text{A11})$$

Therefore, the difference in the nonlocal resistance between quantum axis pointing in $\hat{\mathbf{n}}_p$ and quantum axis pointing in $-\hat{\mathbf{n}}_p$ is given by:

$$\Delta R_{\text{nl}}(x) = R_0 C_{\text{inj}} e^{-\tilde{q} \cos \theta_L x} f(\hat{\mathbf{n}}_p, \omega_L), \quad (\text{A12})$$

where the dimensionless factors $f(\hat{\mathbf{n}}_p, \omega_L)$ and C_{inj} read:

$$f(\hat{\mathbf{n}}_{\mathbf{p}}, \omega_L) = \left\{ \left[-\theta_{\text{sH}} \tilde{q} l_s \cos \theta_p - \frac{l_s}{l_{\text{DMC}}} (\sin \theta_L \cos \theta_p + \sin \theta_p \cos \varphi_p \cos \theta_L) \right] \cos [(l_R^{-1} - \tilde{q} \sin \theta_L) x] \right. \\ \left. + \left[-\theta_{\text{sH}} \tilde{q} l_s \sin \theta_p \cos \varphi_p + \frac{l_s}{l_{\text{DMC}}} (\cos \theta_L \cos \theta_p - \sin \theta_p \cos \varphi_p \sin \theta_L) \right] \sin [(l_R^{-1} - \tilde{q} \sin \theta_L) x] \right\} \quad (\text{A13})$$

$$C_{\text{inj}} = \frac{2 \left(\frac{G}{G_F} P_F \frac{1-P_J^2}{1-P_F^2} + P_J \right)}{\frac{2G_N}{G_F} \left[1 + \frac{G}{G_F} \frac{1-P_J^2}{1-P_F^2} \right] \tilde{q} l_s + \frac{G}{G_F} (1-P_J^2) [\cos \theta_L + (\tilde{q} l_s - \cos \theta_L) \sin^2 \theta_p \sin^2 \varphi_p]} \quad (\text{A14})$$

where $\theta_L = \frac{1}{2} \tan^{-1} [\omega_L \tau_s / (1 - l_s^2/l_R^2)]$, $\tilde{q} l_s = [(1 - l_s^2/l_R^2)^2 + (\omega_L \tau_s)^2]^{1/4}$, $G_F = A_J \sigma_F / \lambda_F$ is the conductance of the ferromagnet, $P_J = |G^\uparrow - G^\downarrow| / G$ is the interfacial current polarization, $P_F = (\sigma_F^\uparrow - \sigma_F^\downarrow) / (\sigma_F^\uparrow + \sigma_F^\downarrow)$ is the current polarization

of the ferromagnetic metal, $G_N = w \sigma_N / l_s$ is the characteristic conductance of the 2D metal, and $G = G^\uparrow + G^\downarrow$ is the total interfacial conductance. Note that we track to all order in the conversion factors (θ_{sH} , l_s/l_{DMC} , l_s/l_R) here and only track to the first order in every conversion factor in the main text.

Lastly, $\Delta R_{\text{nl}}(x)$ can be decomposed into the SHE, EE, and DMC contributions:

$$\Delta R_{\text{nl,sH}}(x) = \frac{2wD}{I\sigma_N} \theta_{\text{sH}} \partial_x s^z \\ = R_0 C_{\text{inj}} e^{-\tilde{q} \cos \theta_L x} \left\{ \left[-\theta_{\text{sH}} \tilde{q} l_s \cos \theta_p + \frac{\theta_{\text{sH}} l_s}{l_R} (\sin \theta_L \cos \theta_p + \sin \theta_p \cos \varphi_p \cos \theta_L) \right] \cos [(l_R^{-1} - \tilde{q} \sin \theta_L) x] \right. \\ \left. + \left[-\theta_{\text{sH}} \tilde{q} l_s \sin \theta_p \cos \varphi_p - \frac{\theta_{\text{sH}} l_s}{l_R} (\cos \theta_L \cos \theta_p - \sin \theta_p \cos \varphi_p \sin \theta_L) \right] \sin [(l_R^{-1} - \tilde{q} \sin \theta_L) x] \right\} \quad (\text{A15})$$

$$\Delta R_{\text{nl,EE}}(x) = -\frac{2wD}{I\sigma_N} \theta_{\text{sH}} l_R^{-1} s^x \\ = R_0 C_{\text{inj}} e^{-\tilde{q} \cos \theta_L x} \left\{ -\frac{\theta_{\text{sH}} l_s}{l_R} (\sin \theta_L \cos \theta_p + \sin \theta_p \cos \varphi_p \cos \theta_L) \cos [(l_R^{-1} - \tilde{q} \sin \theta_L) x] \right. \\ \left. + \frac{\theta_{\text{sH}} l_s}{l_R} (\cos \theta_L \cos \theta_p - \sin \theta_p \cos \varphi_p \sin \theta_L) \sin [(l_R^{-1} - \tilde{q} \sin \theta_L) x] \right\} \quad (\text{A16})$$

$$\Delta R_{\text{nl,DMC}}(x) = -\frac{2wD}{I\sigma_N} l_{\text{DMC}}^{-1} s^x \\ = R_0 C_{\text{inj}} e^{-\tilde{q} \cos \theta_L x} \left\{ -\frac{l_s}{l_{\text{DMC}}} (\sin \theta_L \cos \theta_p + \sin \theta_p \cos \varphi_p \cos \theta_L) \cos [(l_R^{-1} - \tilde{q} \sin \theta_L) x] \right. \\ \left. + \frac{l_s}{l_{\text{DMC}}} (\cos \theta_L \cos \theta_p - \sin \theta_p \cos \varphi_p \sin \theta_L) \sin [(l_R^{-1} - \tilde{q} \sin \theta_L) x] \right\} \quad (\text{A17})$$

Appendix B: Scattering rates and Sources

The source term $\mathcal{Q}(\mathbf{r}, t)$ on the right-hand side of the equation for the spin density (cf. Eq. (43)) is given by

the following expressions:

$$\mathcal{Q}^x(\mathbf{r}, t) = -\frac{s^x(\mathbf{r}, t)}{\tau_{\text{EY}}} - 2\alpha_{\text{asp}} \frac{J_y(\mathbf{r}, t)}{v_F} - 2\alpha_{\text{R}} \frac{J_x^z(\mathbf{r}, t)}{v_F} \quad (\text{B1})$$

$$Q^y(\mathbf{r}, t) = -\frac{s^y(\mathbf{r}, t)}{\tau_{\text{EY}}} + 2\alpha_{\text{asp}} \frac{J_x(\mathbf{r}, t)}{v_F} - 2\alpha_{\text{R}} \frac{\mathcal{J}_y^z(\mathbf{r}, t)}{v_F} \quad (\text{B2})$$

$$Q^z(\mathbf{r}, t) = -\frac{s^z(\mathbf{r}, t)}{\tau_{\text{EY}}^\perp} + 2\alpha_{\text{R}}^\perp \left(\frac{\mathcal{J}_x^x(\mathbf{r}, t)}{v_F} + \frac{\mathcal{J}_y^y(\mathbf{r}, t)}{v_F} \right) \quad (\text{B3})$$

Next, the source term $\chi_i^a(\mathbf{r}, t)$ of the time-evolution equation of the spin density (cf. Eq. (45)) is given by the following expressions:

$$\chi_x^z(\mathbf{r}, t) = -\frac{\mathcal{J}_x^z(\mathbf{r}, t)}{\tau_c} + \alpha_{\text{sk}} J_y(\mathbf{r}, t) + \alpha_{\text{R}} v_F s^x(\mathbf{r}, t) \quad (\text{B4})$$

$$\chi_y^z(\mathbf{r}, t) = -\frac{\mathcal{J}_y^z(\mathbf{r}, t)}{\tau_c} - \alpha_{\text{sk}} J_x(\mathbf{r}, t) + \alpha_{\text{R}} v_F s^y(\mathbf{r}, t) \quad (\text{B5})$$

$$\chi_x^x(\mathbf{r}, t) = -\frac{\mathcal{J}_x^x(\mathbf{r}, t)}{\tau_c'} - \alpha_{\text{R}}^\perp v_F s^z(\mathbf{r}, t) - \alpha_{\text{LD}} \mathcal{J}_y^y(\mathbf{r}, t) \quad (\text{B6})$$

$$\chi_y^y(\mathbf{r}, t) = -\frac{\mathcal{J}_y^y(\mathbf{r}, t)}{\tau_c'} - \alpha_{\text{R}}^\perp v_F s^z(\mathbf{r}, t) - \alpha_{\text{LD}} \mathcal{J}_x^x(\mathbf{r}, t) \quad (\text{B7})$$

$$\chi_x^y(\mathbf{r}, t) = -\frac{\mathcal{J}_x^y(\mathbf{r}, t)}{\tau_c''} + \alpha_{\text{LD}}^\perp \mathcal{J}_y^x(\mathbf{r}, t) \quad (\text{B8})$$

$$\chi_y^x(\mathbf{r}, t) = -\frac{\mathcal{J}_y^x(\mathbf{r}, t)}{\tau_c''} + \alpha_{\text{LD}}^\perp \mathcal{J}_x^y(\mathbf{r}, t) \quad (\text{B9})$$

Finally, in terms of the quantum mechanical amplitudes for scattering with a single impurity, the various scattering and relaxation rates are given by the following expressions:

$$\alpha_{\text{asp}} = \frac{-2\pi n_{\text{imp}}}{\hbar} N_0 \text{Re}(\gamma_I \gamma_R^*) \quad (\text{B10})$$

$$\alpha_{\text{sk}} = \frac{\pi n_{\text{imp}}}{\hbar} N_0 \text{Im}(\gamma_I \gamma_0^*) \quad (\text{B11})$$

$$\alpha_{\text{R}} = \frac{n_{\text{imp}}}{\hbar} [\text{Re}(\gamma_R) + \pi N_0 \text{Im}((\gamma_0 + \gamma_I) \gamma_R^*)] \quad (\text{B12})$$

$$\alpha_{\text{R}}^\perp = \frac{n_{\text{imp}}}{\hbar} [\text{Re}(\gamma_R) + \pi N_0 \text{Im}((\gamma_0 - \gamma_I) \gamma_R^*)] \quad (\text{B13})$$

$$\frac{1}{\tau_c} = \frac{\pi n_{\text{imp}}}{2\hbar} N_0 [|\gamma_0|^2 + 3|\gamma_I|^2 + 4|\gamma_R|^2] \quad (\text{B14})$$

$$\frac{1}{\tau_c'} = \frac{\pi n_{\text{imp}}}{2\hbar} N_0 [|\gamma_0|^2 + |\gamma_I|^2 + 6|\gamma_R|^2] \quad (\text{B15})$$

$$\frac{1}{\tau_c''} = \frac{\pi n_{\text{imp}}}{2\hbar} N_0 [|\gamma_0|^2 + |\gamma_I|^2 + 2|\gamma_R|^2] \quad (\text{B16})$$

$$\frac{1}{\tau_{\text{EY}}} = \frac{2\pi n_{\text{imp}}}{\hbar} N_0 (|\gamma_I|^2 + |\gamma_R|^2) \quad (\text{B17})$$

$$\frac{1}{\tau_{\text{EY}}^\perp} = \frac{4\pi n_{\text{imp}}}{\hbar} N_0 |\gamma_R|^2 \quad (\text{B18})$$

$$\alpha_{\text{LD}} = \frac{\pi n_{\text{imp}}}{\hbar} N_0 [\text{Re}(\gamma_0 \gamma_I^*) + |\gamma_R|^2] \quad (\text{B19})$$

$$\alpha_{\text{LD}}^\perp = \frac{\pi n_{\text{imp}}}{\hbar} N_0 [\text{Re}(\gamma_0 \gamma_I^*) - |\gamma_R|^2] \quad (\text{B20})$$

-
- [1] A. K Geim, and I. V. Grigorieva, *Nature*, **499**, 419 (2013).
 - [2] M. Yankowitz *et al.* Emergence of superlattice Dirac points in graphene on hexagonal boron nitride. *Nature Physics* **8**, 382 (2012).
 - [3] L. A. Ponomarenko *et al.* Cloning of Dirac fermions in graphene superlattices. *Nature* **497**, 594 (2013).
 - [4] C. R. Dean *et al.* Hofstadter's butterfly and the fractal quantum Hall effect in moiré superlattices. *Nature* **497**, 598 (2013).
 - [5] Y. Cao *et al.* *Nature* **556**, 80 (2018).
 - [6] M. Yankowitz *et al.* 10.1126/science.aav1910 (2019).
 - [7] P. Rivera *et al.* Observation of long-lived interlayer excitons in monolayer MoSe2–WSe2 heterostructures. *Nature Comm.* **6**, 6242 (2015).
 - [8] Matthew Yankowitz, Qiong Ma, Pablo Jarillo-Herrero, and Brian J. LeRoy. van der Waals heterostructures combining graphene and hexagonal boron nitride. *Nature Reviews Physics* **1**, 112 (2019).
 - [9] A. Soumyanarayanan, N. Reyren, A. Fert and C. Panagopoulos. Emergent phenomena induced by spin-orbit coupling at surfaces and interfaces. *Nature* **539**, 509 (2016).
 - [10] A. Avsar, J.Y. Tan, T. Taychatanapat, J. Balakrishnan, G.K.W. Koon, Y. Yeo, J. Lahiri, A. Carvalho, A.S. Rodin, E.C.T. O'Farrell, G. Eda, A.H.C. Neto, and B. Ozyilmaz. Spin-orbit proximity effect in graphene. *Nat. Commun.* **5**, 4875 (2014).
 - [11] M. Gmitra, D. Kochan, P. Hiçoçgl, and J. Fabian. Trivial and inverted Dirac bands and the emergence of quantum spin Hall states in graphene on transition-metal dichalcogenides. *Phys. Rev. B* **93**, 155104 (2016).
 - [12] J. Balakrishnan, G. K.W.Koon, A. Avsar, Y. Ho, J. H. Lee, M. Jaiswal, S.-J. Baeck, J.-H. Ahn, A. Ferreira, M. A. Cazalilla, and A. H. Castro Neto, *Nat. Commun.* **5**, 4748 (2014).
 - [13] Z. Wang, D.-K. Ki, H. Chen, H. Berger, A. H. MacDonald, and A. F. Morpurgo, Strong interface-induced spin-orbit interaction in graphene on WS2, *Nat. Commun.* **6**, 8339 (2015).

- [14] A. M. Alsharari, M. M. Asmar, S. E. Ulloa. Topological phases and twisting of graphene on a dichalcogenide monolayer. *Phys. Rev. B* **98**, 195129 (2018)
- [15] Z. Wang, *et al.*, Origin and Magnitude of ‘Designer’ Spin-Orbit Interaction in Graphene on Semiconducting Transition Metal Dichalcogenides, *Phys. Rev. X* **6**, 041020 (2016).
- [16] T. Volkl, T. Rockinger, M. Drienovsky, K. Watanabe, T. Taniguchi, D. Weiss, and J. Eroms, Magnetotransport in heterostructures of transition metal dichalcogenides and graphene. *Phys. Rev. B* **96**, 125405 (2017).
- [17] B. Yang, M. Lohmann, D. Barroso, I. Liao, Z. Lin, Y. Liu, L. Bartels, K. Watanabe, T. Taniguchi, and J. Shi, Strong electron-hole symmetric Rashba spin-orbit coupling in graphene/monolayer transition metal dichalcogenide heterostructures. *Phys. Rev. B* **96**, 041409 (2017).
- [18] T. Wakamura, F. Reale, P. Palczynski, S. Guiz̧eron, C. Mattevi, and H. Bouchiat, Strong Anisotropic Spin-Orbit Interaction Induced in Graphene by Monolayer WS₂. *Phys. Rev. Lett.* **120** 106802 (2018).
- [19] S. Omar and B. J. van Wees, Spin transport in high-mobility graphene on WS₂ substrate with electric-field tunable proximity spin-orbit interaction, *Phys. Rev. B* **97** 045414 (2018).
- [20] A. Avsar, *et al.*, Optospintronics in Graphene via Proximity Coupling, *ACS Nano* **11**, 11678 (2017).
- [21] T. S. Ghiasi, J. I.-Ayni̧oes, A. A. Kaverzin, and Bart J. van Wees, Large Proximity-Induced Spin Lifetime Anisotropy in Transition-Metal Dichalcogenide/Graphene Heterostructures, *Nano Lett.* **17**, 7528 (2017).
- [22] L. A. Benitez, *et al.*, Strongly anisotropic spin relaxation in graphene-transition metal dichalcogenide heterostructures at room temperature, *Nature Physics* **14**, 303 (2018).
- [23] M. Offidani and A. Ferreira, Microscopic theory of spin relaxation anisotropy in graphene with proximity-induced spin-orbit coupling. *Phys. Rev. B* **98**, 245408 (2018).
- [24] J. H. Garcia, M. Vila, A. W. Cummings, and S. Roche. Spin transport in graphene/transition metal dichalcogenide heterostructures. *Chem. Soc. Rev.* **47**, 3359 (2018).
- [25] E. I. Rashba, Graphene with structure-induced spin-orbit coupling: Spin-polarized states, spin zero modes, and quantum Hall effect. *Phys. Rev. B* **79**, 161409 (2009).
- [26] M. Milletari, and A. Ferreira, Quantum diagrammatic theory of the extrinsic spin Hall effect in graphene. *Phys. Rev. B* **94**, 134202 (2016).
- [27] M. Milletari, and A. Ferreira. Crossover to the anomalous quantum regime in the extrinsic spin Hall effect of graphene. *Phys. Rev. B* **94**, 201402(R) (2016).
- [28] Chunli Huang, Mirco Milletari, and Miguel A. Cazalilla. Spin-charge conversion in disordered two-dimensional electron gases lacking inversion symmetry *Phys. Rev. B* **96**, 205305 (2017).
- [29] M. Milletari, M. Offidani, A. Ferreira, and R. Raimondi. Covariant Conservation Laws and the Spin Hall Effect in Dirac-Rashba Systems. *Phys. Rev. Lett.* **119**, 246801 (2017).
- [30] M. Offidani, M. Milletari, R. Raimondi, and A. Ferreira, *Phys. Rev. Lett.* **119**, 196801 (2017).
- [31] M. Offidani, R. Raimondi, and A. Ferreira, *MDPI Condensed Matter* **3**(2), 18 (2018).
- [32] A. H. Castro Neto and F. Guinea. Impurity-Induced Spin-Orbit Coupling in Graphene, *Phys. Rev. Lett.* **103**, 026804 (2009)
- [33] D. V. Fedorov, et al. Impact of Electron-Impurity Scattering on the Spin Relaxation Time in Graphene: A First-Principles Study. *Phys. Rev. Lett.* **110**, 156602 (2013).
- [34] M. Gmitra, D. Kochan, and J. Fabian, *Phys. Rev. Lett.* **110**, 246602 (2013).
- [35] A. Ferreira, T. G. Rappoport, M. A. Cazalilla, and A. H. Castro Neto, Extrinsic Spin Hall Effect Induced by Resonant Skew Scattering in Graphene, *Phys. Rev. Lett.* **112**, 066601 (2014).
- [36] M. Ben Shalom, *et al.*, *Nature Physics* **12**, 318-322 (2016).
- [37] Z. Wang, C. Tang, R. Sachs, Y. Barlas, and Jing Shi, *Phys. Rev. Lett.*, **114**, 016603 (2015).
- [38] C. Huang, Y. D. Chong, and M. A. Cazalilla, *Phys. Rev. B*, **94**, 085414 (2016).
- [39] C. Huang, Y. D. Chong, and M. A. Cazalilla, *Phys. Rev. Lett.* **119**, 136804 (2017).
- [40] Y. K. Luo, *et al.*, *Nano Letters* **17**(6), 3877-3883 (2017).
- [41] R. Raimondi, P. Schwab, C. Gorini, and G. Vignale, *Annalen der Physik* **524**, 3-4 (2012).
- [42] K. Shen, R. Raimondi, and G. Vignale, *Phys. Rev. B* **90**, 245302 (2014).
- [43] X. P. Zhang, C. Huang, and M. A. Cazalilla, *2D Materials* **4**, 024007 (2017).
- [44] A. Burkov, A. S. Nunez, and A. H. MacDonald, *Phys. Rev. B* **70**, 155308 (2004).
- [45] Y.-H. Lin, M. Offidani, C. Huang, M. A. Cazalilla, and A. Ferreira, preprint arXiv:1906.10448 (2019)
- [46] E. I. Rashba, *Sov. Phys. Solid State* **2**, 1109 (1960); E. L. Ivchenko and G. E. Pikus, *JETP Lett.* **27**, 604 (1978); Y. B. Lyanda-Geller, and G. E. Pikus, *JETP Lett.* **50**, 175 (1989); A.G. Aronov and Y.B. Lyanda-Geller, *JETP Lett.* **50**, 431 (1989); V.M. Edelstein, *Solid State Commun.* **73**, 233 (1990).
- [47] J. Rammer, *Quantum Transport Theory*, Vol. 99. Westview Press (2004).
- [48] C. Di Castro, and R. Raimondi, *Statistical Condensed Matter Physics*, Cambridge University Press, (2015).
- [49] Gmitra Martin and Jaroslav Fabian, *Phys. Rev. B* **92** 155403 (2015)
- [50] S. Takahashi and S. Maekawa, *Phys. Rev. B* **67**, 052409 (2003)
- [51] C. Huang, I. Tokatly, and S. Bergeret, *Phys. Rev. B* **98**, 144515, (2018)
- [52] K. Shen, G. Vignale, and R. Raimondi. *Phys. Rev. Lett.* **112**, 096601, (2014)
- [53] F. S. Bergeret and I. V. Tokatly. *Phys. Rev. B* **89**, 134517 (2014)
- [54] F. S. Bergeret and I. V. Tokatly. *Phys. Rev. B* **94**, 180502(R), (2016)
- [55] A. A. Burkov and D. G. Hawthorn. *Phys. Rev. Lett.* **105**, 066802, (2010)
- [56] T. P. Cysne, A. Ferreira, and T. G. Rappoport. *Phys. Rev. B* **98** 045407 (2018).
- [57] F. Calleja, et al. *Nature Physics.* **11**, 43 (2015).
- [58] Maria B. Lifshits and Michel I. Dyakonov *Phys. Rev. Lett.* **103**, 186601, (2009)
- [59] Olga V. Dimitrova *Phys. Rev. B* **71**, 245327, (2005)
- [60] Glazov, M. M., E. Ya Sherman, and V. K. Dugaev. *Physica E: Low-dimensional Systems and Nanostructures* **42**, 9

- (2010): 2157-2177.
- [61] Sherman, E. Ya. "Random spin-orbit coupling and spin relaxation in symmetric quantum wells." *Applied physics letters* 82.2 (2003): 209-211.
- [62] Valenzuela, Sergio O., and M. Tinkham. "Direct electronic measurement of the spin Hall effect." *Nature* 442.7099 (2006): 176.
- [63] R.J. Soulen, Jr. et al., *Science* 282, (85) (1998).
- [64] S. Dubois et al., *Phys. Rev. B* 60, 477 (1999).
- [65] F.J. Jedema, A.T. Filip, and B.J. van Wees, *Nature*(London) 410, 345 (2001)
- [66] In this section, we consider the Rashba model and not the Dirac-Rashba model for graphene since the sub-lattice pseudospin degree of freedom is not important when the Fermi energy is large.
- [67] Note this intrinsic spin Hall effect is *not* a result of summation of the band Berry curvature.